Proceedings of the ASME 2010 3rd Joint US-European Fluids Engineering Summer Meeting and 8th International Conference on Nanochannels, Microchannels, and Minichannels
FEDSM-ICNMM2010
August 1-5, 2010, Montreal, Canada

FEDSM-ICNMM2010-30526

CHARACTERIZATION OF CAPILLARY FLOW WITHIN A HOMOGENOUSLY DISPERSED ARRAY OF VERTICAL MICROPILLARS

Conan Zhang
The University of Texas at Austin
Austin, TX, USA

Carlos H. Hidrovo
The University of Texas at Austin
Austin, TX, USA

ABSTRACT

When considering fluidic devices at the micron length scale, surface tension forces become dominant relative to body forces. Albeit smaller than mechanical and electrical pumps, capillary forces are commonly exploited as a mechanism to drive fluid flow. Unlike pumps, capillary driven flows are passive in nature and are not dependent on auxiliary equipment to drive fluid flow. Although beneficial from an energy standpoint, the lack of a supplementary driving potential causes the flow to be limited by the wick structure dimensions that generate the capillary forces. Subsequently, investigation into the contributions of the wick structure must be performed in order to optimize the fluid flow through a capillary structure.

General capillary theory states that capillary forces increase inversely proportional to the pore radius. Consequently, arrays of vertically aligned nanopillars grown on silicon substrates are considered for fluid flow optimization due to their small pores. To simulate these nanopillars, an *ab initio* analysis was done on a homogenously dispersed array of vertically aligned pillars. An analytical solution to predict the maximum achievable capillary flow with respect to the structure dimensions was found through this method. Subsequently, this analytical solution can be used to produce a set of optimal geometric conditions that would induce the maximum capillary flow through a wick comprised of vertically aligned pillars.

Experimental results are also presented to validate the analytical solution. Homogeneously dispersed cylindrical pillars were created on silicon wafers via reactive ion etching to reconstruct the geometry assumed by the analytical solution. The capillary limit was found for structures with varying geometric dimensions. By contrasting the empirical data with the values predicted by the analytical model, the validity of the analytical model was found to be in good agreement.

INTRODUCTION

Motivation

With the advent of microelectronics and increasing transistor count as dictated by Moore's Law [1, 2], an increase of transistor density is inevitable. Given that transistors generate considerable amounts of heat, heat dissipation becomes a major issue for microelectronics. Currently, many electronics utilize heat pipes for managing heat loads. Due to their passive nature, heat pipes are also ideal for microelectronics. Operating without auxiliary power consumption and pumps, they are efficient and are ideal for compact electronics. However, it is theorized that current heat pipe technology is not capable of handling heat fluxes greater than 100 W/cm^2 with tight temperature control [3]. With the heat flux of electronics projected to increase significantly within the next few years to 100 W/cm^2, it is important to resolve the cooling issue associated with heat pipes promptly [4].

Heat Pipe Limitations

Since heat pipes are passive devices which do not utilize external driving forces, their flow rates are limited by their physical attributes. Depending on the heat pipe design and operation conditions, the source of limitation varies. Common limitations found in heat pipe design include boiling, entrainment, sonic, viscous and capillary limits. Since there are no external driving forces to overcome these limitations, these limits play an important role in heat pipe design. At higher heat fluxes, the heat pipe approaches one of these limits and can no longer provide the evaporator with an adequate amount of fluid necessary for latent heat removal. When this occurs the heat pipe is said to experience dryout.

In moderate heat pipes, such as those used for electronics cooling, the capillary limit is the primary limitation. In high temperature applications with liquid metals, the sonic and entrainment limits become important while viscous limits

become important at cryogenic temperature [5-7]. Another heat pipe limitation that afflicts heat pipes are various temperature ranges is the boiling limit. Since it is often difficult to characterize boiling, most heat pipes are engineered to operate at temperatures much lower than its boiling limit. In order to explore all limitations associated with moderate temperature heat pipes, the boiling limit would be investigated in this paper for completeness. However, the primary focus of this paper would be to focus on the capillary limit of the wick structure via analytical and experimental methods.

Previous Work

In an attempt to address the capillary limit, there has been an increase of interest in the use of nano and micropillars as a wicking structure to optimize capillary flow [8-11]. Although these authors analyze the flow through an array of pillars, they do not address geometric optimization issues. In order to provide a comprehensive understanding of capillary flow, a theoretical model relating fluid flow and pillar geometry must be presented.

Darcy's law is the predominant technique to characterize porous structure in current literature [12]. The basis of Darcy's law is a constitutional characterization of flow rate as a function of permeability of the porous structure. However, the permeability constant is typically based on empirical data and is known for a unique geometry. Since the intent of this paper is to develop a robust model for fluid flow for any given geometry of vertical pillars, an *ab initio* approach must be utilized. Washburn proposed an analytical model based on first principles simulating flow through a capillary tube in 1921 [13]. However, Washburn's model was developed for a capillary tube and not for an array of vertical pillars. For an array composed of nanopillars, the pillar height is typically much greater than the spacing between the pillars yielding a high aspect ratio. Subsequently, the fluid flow involved in a forest of pillars is considerably different from a Hagen-Poiseuille flow through a capillary tube. As a result, an analytical model similar to Washburn's model is performed for an array of pillars shown in Figure 1 to yield an analytical solution to characterize flow as a function of pillar geometry.

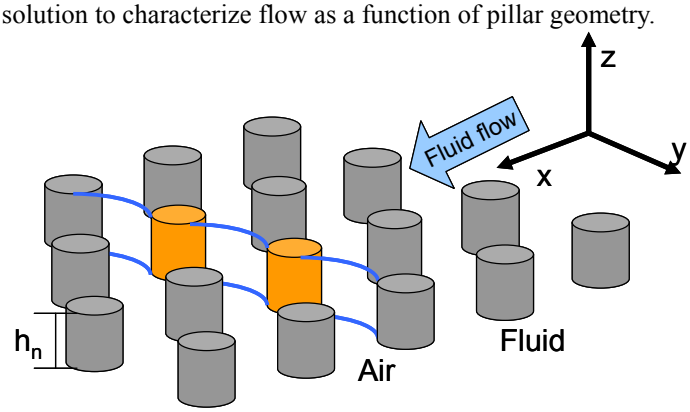

Figure 1. Geometric structure of an array of pillars

Scope of Study

This paper presents an analytical model based on first principles that relates capillary flow to the geometric features of a pillar array. The capillary model is further investigated to yield a permeability constant based on Darcy's law. To supplement the capillary limit model, a boiling model derivated from mass transfer principles is presented to address the other heat pipe limitation observed in moderate temperature heat pipes.

Experimental data is also presented to corroborate the analytical model. In an attempt to concentrate solely on the wick structure, only the wick is examined and the condenser and vapor void portion of a typical heat pipe is neglected by exposing the wick to ambient conditions. The pillars were produced via photolithography on silicon wafers creating a homogenous wick comprised of uniformly dispersed pillars.

NOMENCLATURE

δ	Fluid inflection distance inward
κ	Permeability constant
θ	Contact angle of fluid on solid interface
μ	Dynamic viscosity of the fluid
ρ	Density of the fluid
σ	Surface tension of fluid
A_c	Cross sectional area of fluid flow
A_{surf}	Surface area
c_p	Specific heat capacity
d_n	Diameter of nanotube pillar
H	Height of fluid at point i
h_{fg}	Heat of formation
h_{air}	Heat transfer coefficient of air
h_{water}	Heat transfer coefficient of water
k	Thermal conductivity of a solid
L_{wick}	Length of wick
$\dot{m}$	Mass flow rate
P	Pressure of fluid
q	Heat loss
Q	Volumetric flow rate
r_{eff}	Effective pore radius
R	Radius of curvature
s	Spacing between pillars
T	Temperature
u	Velocity
w_n	Center to center nanotube spacing
w_{wick}	Width of wick sample
x_{Ai}	Molar fraction of species A at location i

THEORETICAL MODEL

Capillary Limit Model

The capillary limit is fundamentally based on the balance of capillary and viscous forces. Capillary force arises from the surface tension of a liquid-solid interface. For a structure given by Figure 2, the Laplace pressure induced by the surface tension forces is given by the equation [6]:

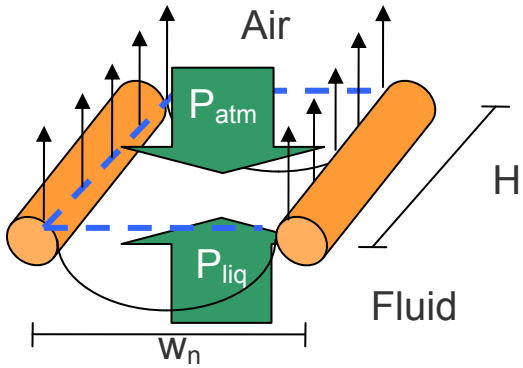

Figure 2. Surface tension forces acting on the liquid-solid interface between two pillars yields a Laplace pressure

$$\Delta P_{cap} = \frac{2\sigma\cos\theta}{w_n} \quad (1)$$

where σ is the surface tension of the interface, θ is the contact angle, w_n is the width or spacing between the nanopillars and ΔP_{cap} is the equivalent capillary pressure induced by the surface tension. For the aforementioned wick composed of pillars, this is typically the only pressure gradient driving fluid flow for a structure with no external influences.

The viscous loss was calculated by approximating the pillars are flat surfaces as shown in Figure 3. Subsequently, this yields two different variations of viscous loss. As shown in Figure 4, region A experiences viscous loss only from the substrate while region B experiences viscous loss similar to a flow within an open channel. Starting from the momentum equation, the velocity profile for the two regions can be found analytically.

With only viscous loss from one dimension in region A, the flow rate is found simply to be [14]:

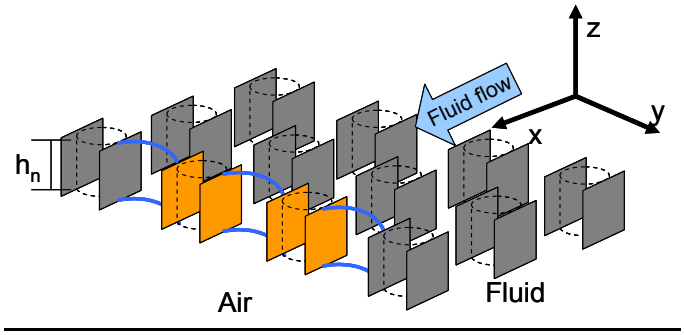

Figure 3. Approximation of pillars as flat plates

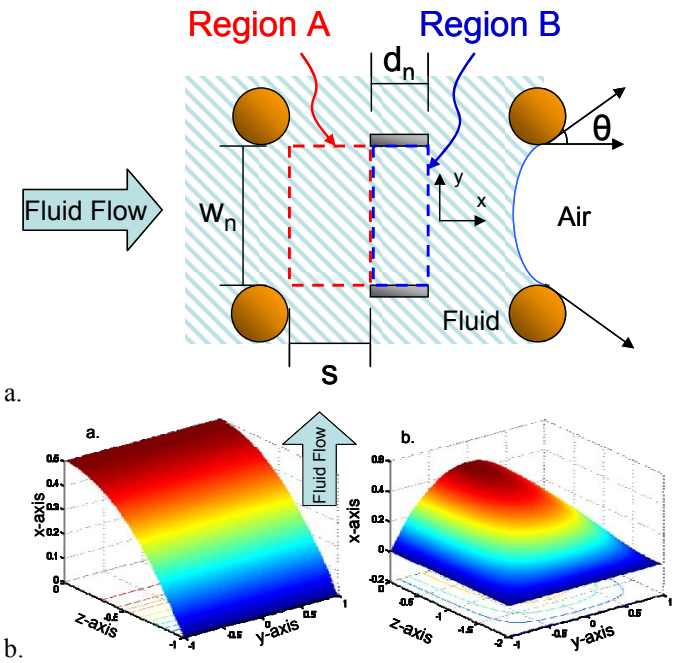

Figure 4. (a) The two different regions of viscous loss and (b) the resultant velocity profile

$$Q_A = \frac{h_n^3 w_n}{3\mu}\frac{\Delta P}{L_{eff,A}} \quad (2)$$

where ΔP is the pressure difference between the two ends of the wick and $L_{eff,A}$ is the effective length of the wick experiencing the one dimensional viscous loss. The pressure loss due to region A can be rearranged to

$$\Delta P_{loss,A} = \frac{3\mu L_{eff,A}}{h_n^3 w_n} Q_{vol} \quad (3)$$

Conversely, the viscous loss associated with region B is more complex and involves viscous loss from two dimensions. The subsequent analytical solution is in the form of a Fourier

series. The solution was nondimensionalized and solved numerically via Matlab to yield an array of nondimensionalized flow rates. From the array, a linear trend line was acquired with respect to the aspect ratio given by

$$Q_B^* = 0.66525a \qquad (4)$$

where a is two times the h_n/w_n. When dimensional variables are reintroduced in this relationship, the pressure loss associated with region B is found to be:

$$\Delta P_{loss,B} = 12.0256\frac{\mu L_{eff,B}}{w_n^3 h_n}Q_{vol} \quad (5)$$

At quasi-steady state conditions, the forces driving the flow would equal the frictional losses over the same length. Assuming that the cross-section of fluid flow remains constant along the length of the wick, a balance of forces yields a flow rate given by

$$Q_{vol} = \left(\frac{3\mu s x}{h_n^3 w_n (d_n + s)} + \frac{12.0256\mu d_n x}{w_n^3 h_n (d_n + s)}\right)^{-1} \frac{2\sigma\cos\theta}{w_n} \quad (6)$$

for a control volume of width w_n.

For a wick of with a width, w_{wick}, and length, L_{wick}, the mass flow rate at the capillary limit can be found by modifying equation (6) with the packing density of the pillars using the following relationship:

$$\dot{m}_{\max} = \rho\left(\frac{w_n}{w_n + d_n} w_{wick}\right)Q_{vol} \quad (7)$$

By comparing equation (6) with Darcy's law, an effective permeability constant can also be found to be given by:

$$\kappa_{eff} = \left(\frac{3s(w_n + d_n)}{w_n h_n^2 (d_n + s)} + \frac{12.0256 d_n (w_n + d_n)}{w_n^3 (d_n + s)}\right)^{-1} \quad (8)$$

Boiling Limit Model

The mass flow at the onset of boiling can also be modeled using fundamental transport phenomena equations. The governing equation for mass diffusion across a flat planar surface is given by [15]:

$$1 + \frac{(N_{A0} + N_{B0})(x_{A0} - x_{A\infty})}{N_{A0} - x_{A0}(N_{A0} + N_{B0})} = \exp\left(\frac{N_{A0} + N_{B0}}{k_{x,loc}}\right) \quad (9)$$

where N_{A0} and N_{B0} are the molar fluxes of water and air across the liquid interface, x_{A0} and $x_{A\infty}$ are the molar fractions of water at the interface and at a distance far away from the interface respectively and $k_{x,loc}$ is the molar diffusivity. Assuming that the molar flux of air into the water is negligible (N_{B0}), equation (9) can be simplified to

$$N_{A0} = k_{x,loc}\ln\left(1 + \frac{x_{A0} - x_{A\infty}}{1 - x_{A0}}\right) \quad (10)$$

The molar fractions (x_{A0} and $x_{A\infty}$) can be obtained via the relationship:

$$x_A = \frac{P_{H_2O}}{P_{total}} \qquad (11)$$

The partial pressure at the interface can be obtained with the relationship [16]:

$$P_{H_2O,0} = 10^{\left(0.6715 + 0.030T_s - 0.0000798T_s^2\right)} \qquad (12)$$

where the P_{H2O} is the partial pressure in units of Torr and T_s is the liquid surface temperature in units of Celsius. The partial pressure far away from the interface can be obtained by humidity readings

$$P_{H_2O,\infty} = \phi P_{sat} \quad (13)$$

where φ is the humidity ratio and P_{sat} is the saturation pressure at a given temperature. At room temperature, the saturation pressure is 3130 Pa.

The molar diffusivity can be obtained from the Sherwood number. Using a mass diffusion analogy for a natural convection flow over a vertical flat plate, the Sherwood number can be found to be [15, 17]:

$$Sh_x = 0.508\left[\frac{Sc}{0.952 + Sc}\right]^{1/4} Ra_x^{1/4} = \frac{k_{x,loc} l_0}{cD_{AB}} \quad (14)$$

or

$$k_{x,loc} = 0.508 \frac{cD_{AB}}{l_0} \left[\frac{Sc}{0.952 + Sc} \right]^{1/4} Ra_x^{1/4}$$

(15)

where c is the total molar concentration, D_{AB} is the diffusivity of the water into the air, l_0 is the characteristic length, Sc is the Schmidt number and Ra is the Raleigh number. The variable c can be found using the ideal gas relation:

$$c = \frac{P}{RT} \qquad (16)$$

and the Raleigh number is given by [17]:

$$Ra = \frac{\beta \left(T_s - T_\infty \right) g x^3}{\upsilon \alpha} \qquad (17)$$

The diffusivity and Schmidt number of water diffusion into air are given to be approximately D_{AB}=0.24*10^{-6} m^2/s and Sc=0.625.

Using equation (10) and the aforementioned relations, the molar flux can be obtained at the onset of boiling. Subsequently, for known surface dimensions, the mass flow can be calculated using the equation:

$$\dot{m} = N_{A0} A_c M \qquad (18)$$

where A_c is the cross sectional area of mass flux and M is the molar mass. Incorporating the evaporation rate with an energy balance, the onset of boiling can be found as a function of heat input. From the law of conservation of energy, the heat input into the wick structure equals the phase change and conduction:

$$\dot{Q} = \dot{m} h_{fg} + k A_c \frac{(T_s - T_{water})}{L_{wick}} \qquad (19)$$

where h_{fg} is the heat of vaporization of water, k is the thermal conductivity of the wick structure and L_{wick} is the length of the wick.

EXPERIMENTAL SETUP

Critical Heat Flux Measurements

In intermediate temperature heat pipes such as those found in electronic devices, the wick's ability to move fluid back to the heat source is typically the limiting factor in heat removal [18]. At high heat fluxes, the wick of a heat pipe would dry out due to the wick's inability to transport fluid back to the heat source. When this heat flux is reached, the superheat of the system increases and the mass flow rate of the fluid ceases to increase with increasing heat input.

To investigate this phenomenon, strips of various wicking materials were exposed to atmospheric conditions in order to reduce the influence of vapor pressure and saturation issues at the liquid interface. One end of the wick was then attached to the face of a copper block extrusion by a low-conduction ceramic frame made of MACOR®. The subsequent portion of the wick that was exposed to the atmosphere and also in contact with the copper block measured to be approximately one square centimeter. The other end of the wick was dipped into a reservoir of distilled water that rests on an analytical balance as shown in Figure 6. Since the wick pulls water upwards away from the reservoir, the water reservoir's mass would change over time. By measuring the mass with respect to time, the mass flow through the wick can be determined. At room temperature, the only mass flow that occurs within a saturated wick is associated with natural evaporation. This unwarranted effect introduces additional sources of mass flow to experimental measurements. The natural evaporation rate is subtracted from subsequent mass flow measurements with heat fluxes to negate this effect. A heat flux was provided by the copper block through resistance heating to induce a mass flow through the wick. Since most of the copper block is wrapped with mineral wool, the majority of the heat is directed towards the wick interface that is exposed to the air.

The heat input to the system was controlled with a variable autotransformer for high wattages and a DC power supply for wattages less than 2.9 W to reduce uncertainty associated with the instruments. At each wattage setting, samples were taken every two or four seconds over a 15-minute span. The uncertainties for the measurements were evaluated with respect to a Gaussian distribution as well as the intrinsic instrument errors.

In order to record the wattage used to heat the copper block, a wattage transducer was used to convert the heater power to a 0-10 volt DC signal that was decipherable by LabVIEW as shown in Figure 7. For lower heat fluxes (primarily used for nanowicks), a DC power supply was used in place of the variable autotransformer. The voltage supplied by the DC power supply was measured by LabVIEW and the current was acquired by measuring the voltage drop over a 5Ω shunt resistor.

The acquisition of the water reservoir's mass was done concurrently on an analytical balance via LabVIEW at four-second sample intervals. The mass flow rate of the wick was found by dividing the variation in mass of the reservoir with time. This mass flow was corrected for evaporation and plotted against the heat flux.

Thermocouples were also placed at various points on the experiment to quantify the enthalpy change of the fluid and the heat loss of the experiment. Since the experimental setup was designed with size limitations in mind, the mineral wool and MACOR® piece did not provide adequate insulation and there are slight heat losses to the environment that must be analyzed

with these thermocouples. The net heat flux exerted on the wick was corrected with these losses.

Heat Loss through Insulation

The sole purpose of the insulation used in the experimental setup was to direct the heat flux towards the wick interface. However, insulation merely reduces the heat transfer between an object and its environment and does not eliminate heat

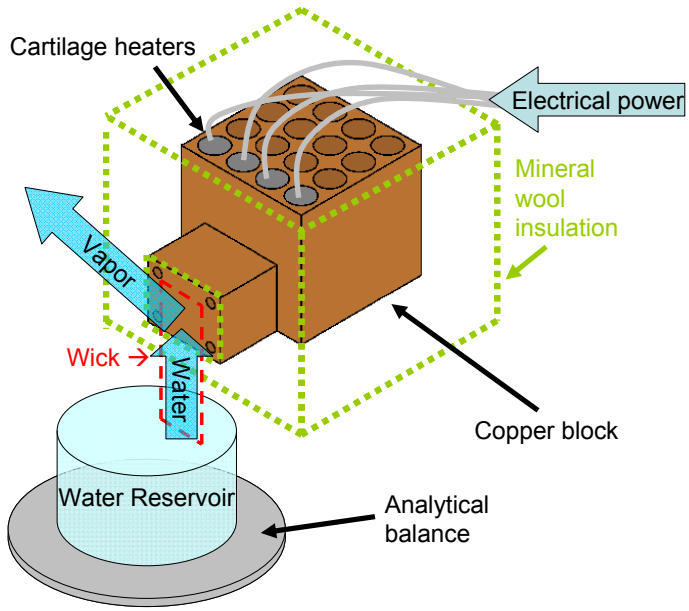

Figure 5. Illustration of experimental setup

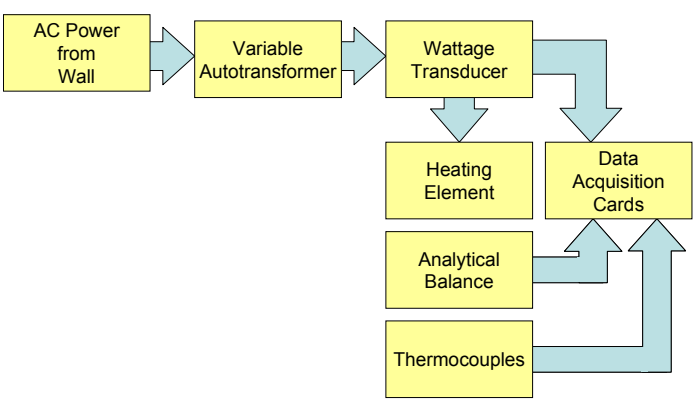

Figure 6. Schematic of experimental setup

transfer. An insulator typically reduces heat loss with increasing thickness and is therefore limited by the maximum dimensions of the experimental design. To account for any possible heat loss through the insulation, thermocouples were placed on both sides of the insulation so that a conduction model could be applied.

Since the insulation thickness was maximized for the experimental setup, the insulation thickness was large relative to the other system dimensions. Consequently, a 1D conduction approximation through the insulation would not be valid due to 2D conduction through the edges and 3D conduction through the corners of the insulation. To simplify the analysis, conduction shape factors were used to approximate the conduction through the edges and corners [17]. Finding the summation of the heat loss through the faces, edges and corners of the insulation, the total heat loss through the insulation can be found and deducted from the heat input to yield an actual heat flux through the wick interface.

Wick Conduction Losses

High conducting metals are typically used for heat pipe wicks and casings in order to increase the heat transfer from the heat source to the condenser. Similar to heat pipes, the wick strips used in the investigation experiences conduction through the wick structure. Since this project investigates the flow associated with capillary forces, it is imperative to deduct the influences of other sources of heat transportation and focus solely on the heat removal associated with the fluid flow.

As Figure 8 shows, a temperature gradient exists along the wick indicating heat transfer does occur through the wick. The section outlined in red was analyzed in order to find the heat transfer rate. The wick can be properly modeled as a rectangular fin resting in two stagnant fluids and experiencing natural convection governed by the equation:

$$q_{convective\_loss} = h_{air} A_{surf,1} \left(\frac{T_{base} + T_{mid}}{2} - T_{air}\right) + h_{water} A_{surf,2} \left(\frac{T_{mid} + T_{water}}{2} - T_{water}\right) \quad (20)$$

where h_{air} and h_{water} are the heat transfer coefficients of the air and water respectively. T_{base} is the temperature at location the wick meets the copper block, T_{mid} is temperature at the interface of the two fluids and T_{water} is the water temperature. Since the water is a highly conductive fluid, the temperature of the water was assumed to be equal to the temperature of the tip of the wick emerged in the reservoir.

Due to the broad range of values for the two heat transfer coefficients, this method provides huge uncertainty values. The heat transfer coefficient for natural convection in air ranges from 10-100 W/m^{2}K. Similarly, the heat transfer coefficient for natural convection in water can range from 500-10,000 W/m^{2}K, which introduces magnitude of 20 difference in the analysis [19]. Considering that phase change is inherent to the system and possible vapor saturation issues may also alter the heat transfer coefficient of the air, formulating heat loss via convection may not generate an accurate value.

An assumption was made that the air served as an insulating fluid with respect to the water reservoir to circumvent the convection-based heat loss analysis. With this

assumption, an 1D conduction model is applied to the wick. Figure 9 depicts the temperature profile along the wick of the analyzed section. The coefficient of determination (R^2) of the linear fit justifies the conduction assumption with a value near unity. The conduction loss can be calculated with the equation [20]:

$$q_{conduction\_loss} = kA_c \frac{dT}{dx} \quad (21)$$

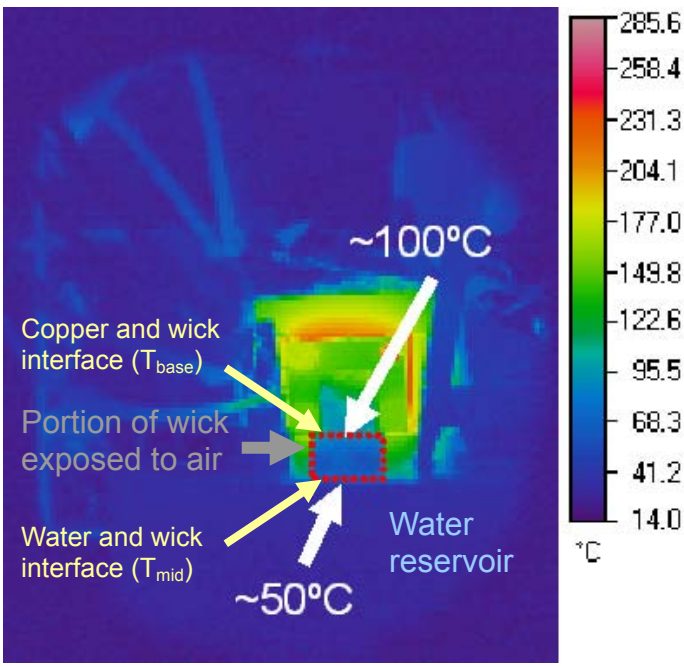

Figure 7. The temperature gradient along the wick can be seen in the thermal IR image of the experimental setup.

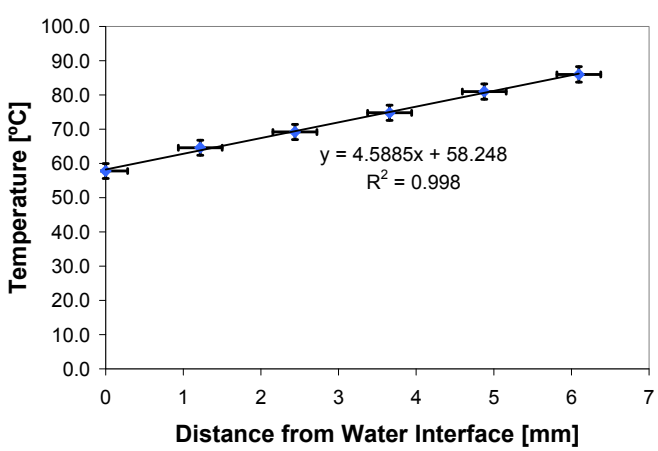

Figure 8. Example of temperature profile over the portion of wick exposed to air

where the k is the thermal conductivity of the wick taken from literature [17, 21]. A_c is the cross-section of the wick obtained by SEM imaging and dT/dx is the temperature distribution extracted from the slope of the linear fit. Although there is inherent uncertainty associated with thermal conductivity, the uncertainty associated with the conductivity is magnitudes lower than the heat transfer coefficients of the two fluids.

Actual Heat Flux through the Wick

Combining the heat losses with the power input to the system, the actual heat loss associated with the wick can be found by the equation:

$$q_{actual} = q_{measured} - q_{insulation} - q_{wick} \quad (22)$$

where q_{actual} is the total heat dissipated by the wick, $q_{measured}$ is the power that was measured to the heaters, $q_{insulation}$ is the calculated heat loss through the insulation and q_{wick} is the heat loss via conduction through the wick. The heat flux exerted on the wick can be calculated by dividing the total heat exerted on the wick with the surface area of the wick that is in contact with heating element.

$$\phi_q = \frac{q_{measured} - q_{insulation} - q_{wick}}{A_{surf,wick}} \quad (23)$$

where Φ_q is the heat flux through the wick and $A_{surf,\text{wick}}$ is the surface area of the wick exposed to a the heated copper block. The heat fluxes capable by the wicks were compared with the theoretical predictions as well as each other.

RESULTS

Experiments were performed on two wicks comprised of 20 µm tall, 30 µm diameter pillars spaced 120 and 160 µm apart. For these two wick samples, experimental data correlated well with the two theoretical models proposed. For the wick spaced 120 µm apart, the onset of boiling was theorized to occur first whereas the capillary limit was expected to occur first in the wick spaced 160 µm apart.

As shown in Figure 9, the mass flow rate ceased to follow the "Corresponding Mass Flow" line when the limit was theorized to occur. Based on the temperature data, the limit that the 120 µm-spaced wick approached was the boiling limit. Conversely, as shown in Figure 10, the data shows that the 160 µm-spaced wick reaches a limit prior to boiling. Consequently, it can be interpreted that this wick has reached the capillary limit prior to the onset of boiling.

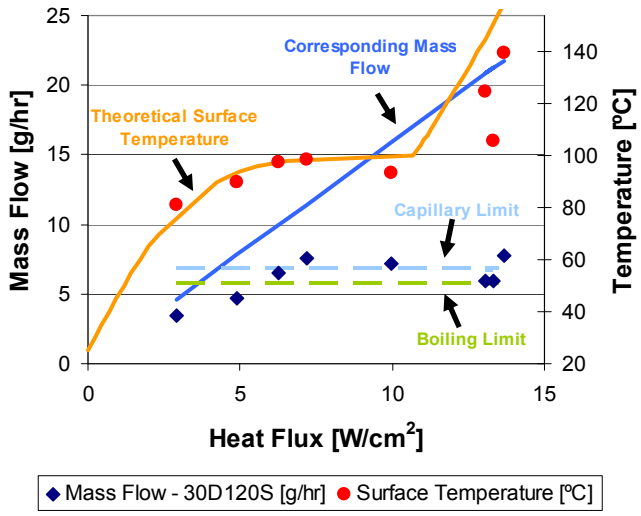

Figure 9. Experimental and theoretical data for a wick of pillars spaced 120 µm apart

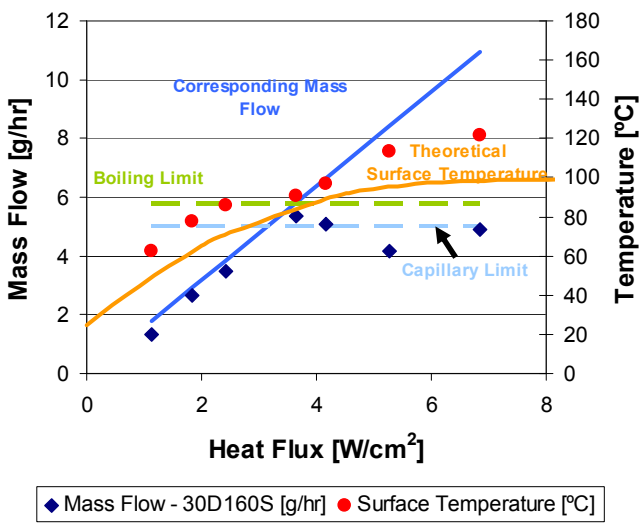

Figure 10. Experimental and theoretical data for a wick of pillars spaced 160 µm apart

CONCLUSIONS

This paper presents two valid models that predict reasonable and accurate heat pipe limitations. Based on first principles, these two models provide a robust representation of heat pipe limitations based on microscopic wick geometries. Although these models were developed with a uniformly dispersed and regular geometry in mind, the models can be extended to non-homogenously dispersed pillar arrays such as carbon nanotubes and silicon nanowires with additional uncertainty [22].

Future research should be performed with the intention of producing a more accurate model of the boiling limit by incorporating the microscopic features of the wick. By considering the microscopic features of the wick as nucleation sites, the boiling limit model can be further enhanced to produce more accurate predictions of the onset of boiling.

REFERENCES

1. Moore, G.E., *Cramming more components onto integrated circuits.* Electronics, 1965. **38**(8).
2. Moore, G.E. *Progress in digital integrated electronics*. in *Electron Devices Meeting, 1975 International*. 1975.
3. Swanson, T.D. and G.C. Birur, *NASA thermal control technologies for robotic spacecraft.* Applied Thermal Engineering, 2003. **23**(9): p. 1055-1065.
4. iNEMI, *Electronics Manufacturing Initiative Technology Roadmap.* 2006.
5. Peterson, G.P., *An introduction to heat pipes : modeling, testing, and applications*. Wiley series in thermal management of microelectronic & electronic systems. 1994, New York: Wiley. xii, 356 p.
6. Reay, D.A., P.A. Kew, and P.D. Dunn, *Heat pipes*. 5th ed. 2006, Oxford ; Burlington, MA: Butterworth-Heinemann. xvii, 377 p.
7. Silverstein, C.C., *Design and technology of heat pipes for cooling and heat exchange*. 1992, Washington, D.C.: Hemisphere Pub. Corp. x, 368 p.
8. A. Bar-Cohen, P.W., E. Rahim, *Thermal Management of High Heat Flux Nanoelectronic Chips.* Microgravity Science and Technology, 2007.
9. Ishino, C., et al., *Wicking within forests of micropillars.* Epl, 2007. **79**(5): p. 5.
10. Jiao, A.J., H.B. Ma, and J.K. Critser, *Heat Transport Characteristics in a Miniature Flat Heat Pipe With Wire Core Wicks.* Journal of Heat Transfer, 2008. **130**(5): p. 6-6.
11. Jijie, J.Z., N. Flavio, and G. Morteza, *Flow conveying and diagnosis with carbon nanotube arrays.* Nanotechnology, 2006. **17**(19): p. 4845-4853.
12. Dormieux, L., D.d. Kondo, and F.J. Ulm, *Microporomechanics*. 2006, Chichester, West Sussex, England ; Hoboken, NJ: Wiley. xvi, 328 p.
13. Washburn, E.W., *The Dynamics of Capillary Flow.* Physical Review, 1921. **17**(3): p. 273.
14. Panton, R.L., *Incompressible flow*. 3rd ed. 2005, Hoboken, N.J.: J. Wiley. xvi, 821 p.
15. Bird, R.B., W.E. Stewart, and E.N. Lightfoot, *Transport phenomena*. Rev. 2nd ed. 2007, New York: J. Wiley. xii, 905 p.
16. Dean, J.A. and N.A. Lange, *Lange's handbook of chemistry*. 15th ed. 1999, New York: McGraw-Hill. 1 v. (various pagings).

17. Mills, A.F., *Heat transfer*. 2nd ed. 1999, Upper Saddle River, N.J.: Prentice Hall. xxii, 954 p.
18. Peterson, G.P., *An introduction to heat pipes : modeling, testing, and applications*. 1994, New York: Wiley. xii, 356 p.
19. Incropera, F.P. and D.P. DeWitt, *Fundamentals of heat and mass transfer*. 5th ed. 2002, New York: J. Wiley. xix, 981 p.
20. Mills, M.P., *The Internet Begins with Coal.* Environment & Climate News, 1999.
21. CINDAS, *Thermophysical Properties of Matter Database (TPMD)*
22. Zhang, C., *Investigation of Nanopillar Wicking Capabilities for Heat Pipe Applications.* Proceedings of ASME 2009 2nd Micro/Nanoscale Heat & Mass Transfer International Conference, 2009.